Acta Oceanol. Sin., 2019, Vol. 38, No. 2, P. 34–43
https://doi.org/10.1007/s13131-018-1273-6
http://www.hyxb.org.cn
E-mail: hyxbe@263.net

Grain size characteristics of the carbonate-free fraction of surface sediments from the Southwest Indian Ridge area and its geological significance

Qi Jia[1], Dejiang Fan[1, 2*], Xiaoxia Sun[1], Ming Liu[1], Wenqiang Zhang[1], Zuosheng Yang[1]

[1] Key Laboratory of Submarine Geosciences and Prospecting Techniques of Ministry of Education, Ocean University of China, Qingdao 266100, China

[2] Laboratory for Marine Geology and Environment, Pilot National Laboratory for Marine Science and Technology (Qingdao), Qingdao 266061, China

Received 5 January 2018; accepted 26 June 2018

Abstract

The carbonate-free fraction of 20 surface sediments collected from the ultraslow-spreading Southwest Indian Ridge (SWIR) was studied by grain size analysis and mineralogical analysis with X-ray powder diffraction (XRD), stereo microscopy and scanning electron microscopy (SEM). The characteristics of the carbonate-free fraction of the sediments were obtained, and related influential factors were discussed. The results show that the mean grain size of this fraction is in 1.96Φ–8.19Φ, with poorly sorting and unimodal, bimodal or irregular bimodal distribution patterns. Four grain size end members of the fraction are derived with the End Member Model method. The finest end member EM1 shows a significant contribution of terrigenous materials of the aeolian input and sediment carried by the bottom current. End member EM2 with medium size mainly reflects sediment of a siliceous bioclast origin. EM3 and EM4 are interpreted as representing the coarser volcanic materials related to bedrock weathering or volcanic activities. Multi-provenance is the dominant factor controlling the grain size pattern of the carbonate-free fraction of the sediments in that area. In addition, sediment transport processes such as the bottom current and wind are the minor factors that influence the grain size distribution of the carbonate-free fraction sediments.

Key words: Southwest Indian Ocean, carbonate-free fraction, grain size distribution pattern, end member model, provenance

Citation: Jia Qi, Fan Dejiang, Sun Xiaoxia, Liu Ming, Zhang Wenqiang, Yang Zuosheng. 2019. Grain size characteristics of the carbonate-free fraction of surface sediments from the Southwest Indian Ridge area and its geological significance. Acta Oceanologica Sinica, 38(2): 34–43, doi: 10.1007/s13131-018-1273-6

1 Introduction

The carbonate-free fraction of sediments is the portion of sediments that contains no carbonate component and is also referred to as the "lithic fraction" (Revel et al., 1996). Compared to the carbonate fraction that usually contributes to the reconstruction of paleoclimatic evolution, although the noncarbonate fraction makes up only a small part of the deep sea sediment composed mainly of calcareous oozes, it is more efficient to record and provides diverse "lithic" information. This sediment fraction has different origins, such as terrestrial, volcanic and ice-rafted sources (McCave et al., 1995), and the lithic particles may be transported into the open ocean through various processes: (1) atmospheric circulation (Rea, 1994); (2) surface circulation (Ruddiman, 1977); (3) hemipelagic processes (turbidity currents) and (4) bottom circulation (Biscaye and Eittreim, 1977). Many studies have confirmed that the carbonate-free fraction in marine sediments can be a good indicator to extract the source message and reconstruct sedimentary processes (Stein et al., 1994; Povea et al., 2015). Likewise, grain-size, as the most fundamental property of sediments, contains useful information about sediment provenance and transport mechanisms (McLaren and Bowles, 1985). In the 1960s, Hails (1967) and Doeglas (1968) discussed the relationship between grain size composition and sedimentary environment. The grain size might also serve as a key index in research on monsoon evolution (An et al., 2001), ocean current changes (McCave and Hall, 2006) and tectonic movement.

The seafloor surface of the Southwest Indian Ridge (SWIR) is predominantly composed of calcareous ooze with a thinner thickness and discontinuous distribution due to its younger age (Bernard et al., 2005) and deeper carbonate compensation depth (CCD) of approximately 4 800 m (Kolla et al., 1976a). With the development of seabed *in situ* testing technology and sampling techniques in the last two decades, an upsurge in exploration for hydrothermal sulfide deposits has appeared in different countries around the world (German et al., 2016). The SWIR is representative of an ultraslow-spreading ridge with high attention, and researches on this area have involved the composition and evolution of hydrothermal plumes and fluids, the mineralogical and geochemical characteristics of both hydrothermal products and surrounding basement rocks, hydrothermal biological processes,

---

Foundation item: China Ocean Mineral Resources Research and Development under contract No. DY125-11-R-04; the National Natural Science Foundation of China under contract No. 41676036.

*Corresponding author, E-mail: djfan@ouc.edu.cn

the mechanism of the hydrothermal system cycle and the flux of heat and mass (Zeng, 2011). Studies of the surface sediments covering oceanic bedrock or mineralized layers, however, are of relatively recent origin and serve largely to give the general reader an initial understanding of sediment material composition, geochemical characteristics and sources (Chen et al., 2013; Huang et al., 2016; Li et al., 2016). In a sedimentary environment as complicated as that of the SWIR, what grain size response will be found in surface sediments of the surrounding area and what geological information is hidden? To the author's knowledge, little research into relevant aspects of similar geomorphic units has been carried, and those studies that exist involve only sediment particle-size partition, the estimation of sedimentation rate (Cronan and Hodkinson, 1997) and the content variation of metal elements such as iron and manganese in different particle sizes (Skornyakova, 1965; Gurvich, 2006). To date, there has been no systematic research report on the geological significance of grain size.

Here, we selected 20 surface sediment samples in the SWIR area, conducted a grain size analysis of the carbonate-free fraction and systematically analyzed the characteristics of grain size distribution patterns and end member constitution. Based on the grain size data combined with the corresponding mineralogical compositions, the lithic provenance of the surface sediments in the SWIR area is presented, and the related sedimentary process signals are revealed. The results are helpful for the exploration of hydrothermal sulfide deposits.

2 Geological background

The SWIR (Fig. 1a), extends 8 000 km from the Rodriguez Triple Junction (RTJ) in the northeast to the Bouvet Triple Junction (BTJ) in the southwest, separating the African and Antarctic plates, and is a typical ultraslow-spreading ridge with a full spreading rate of 14–16 mm/a in a NE-SW direction (Dick et al., 2003). The axis of the SWIR is marked by an oblique spreading and is offset by sets of N-S running transform faults such as the Atlantis II and the Melville FZs. Its surrounding topography varies greatly and has deep axial valleys with water depths deeper than 5 000 m; moreover, it generally lacks magmatic activity (Muller et al., 1999). Basalts are the main outcropping rocks in the SWIR, and mantle materials such as serpentinized peridotites and gabbros are occasionally exposed in the fault regions (Bach et al., 2002; Zhou and Dick, 2013). As seafloor hydrothermal activity survey has continued, seven hydrothermal fields have been discovered and reported in the SWIR, which including the first discovered active field, the 49.6°E hydrothermal field, at 37°47′S, 49°39′E. Furthermore, hydrothermal products were also observed at the 49.26°E, 49.6°E, 51.73°E and 50.5°E hydrothermal fields (Tao et al., 2014).

Our study area is located on the high mound between the In-

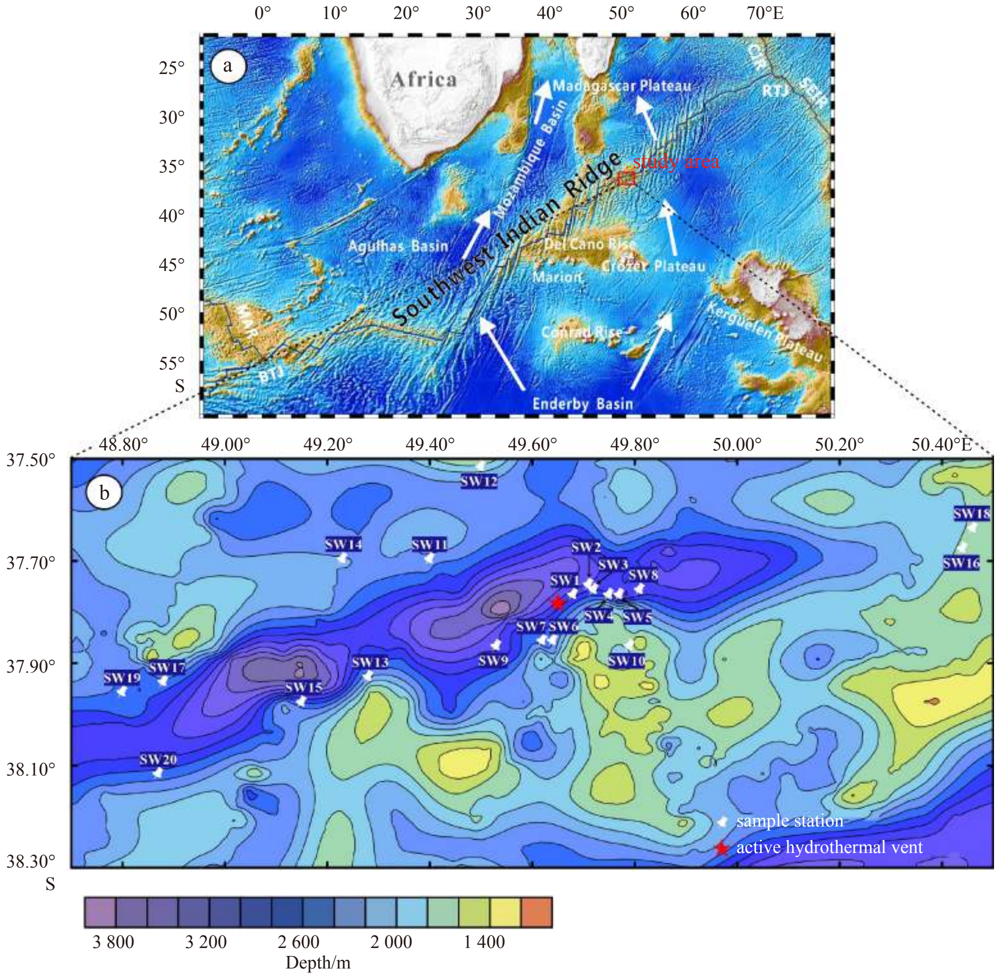

Fig. 1. Map of the study area (a) and sampling location (b). The white arrows point in the direction of the Antarctic bottom current (current data based on Mantyla and Reid (1995)).

domed and the Gallieni FZs. According to Cannat et al. (1999), the ridge segments of this region are divided into Segment 27 (50.5°–49.91°E) and Segments 28–29 (49.91°–48.80°E) from right to left. The volcanic ridge and non-transform discontinuity are often in an opposite arrangement in the axial valley region of Segments 28–29, where the northern flank is characterized by obvious volcanic activities and the southern flank is controlled by tectonic activities. Additionally, the 49.6°E hydrothermal field sits right in the center of this segment. Segment 27 has an abundant magma supply and intense volcanic activities with the lack of axial valley (Liang et al., 2014). The water depths on the south side of ridge axis are generally shallower, with an average of 3 180 m.

The sediments of this area are mainly biogenic components that consist of foraminifera and calcareous nannofossils, with subordinate seafloor volcanic debris and terrigenous material carried by atmospheric circulation and the ocean current. The deep-water bottom current in the study area is represented by the Antarctic Bottom Water (AABW) originating in the Weddell Sea (Mantyla and Reid, 1995). The northward flow of the AABW, heavily controlled by submarine topography, has two main pathways into the Southwest Indian Ocean. (1) On the west, via a gap in the SWIR (50°S, 30°E), the AABW flows into the Agulhas, Natal and Mozambique Basins, and (2) through the Crozet-Kerguelen gap Plateaus (50°S, 60°E), the AABW fills into the Crozet, Madagascar, Mascarene, Somali, and Arabian Basins as a deep western boundary current of the Indian Ocean (Haine et al., 1998). Previous deep-towed and moored investigations near the Longqi vent have found that the bottom water here mainly flows from southeast to northwest with a maximum velocity of 20–30 cm/s (Liao et al., 2016).

3 Materials and methods

During the 34th and 39th Chinese cruises of the R/V *Dayang Yihao*, surface sediment samples were collected using a TV-guided grab sampler from 20 stations in the region of 48.7°–50.5°E of the SWIR. These stations were located at the northern and southern flanks in the vicinity of the SWIR axial zone within a depth range of 1 500–3 200 m. Detailed information about sampling sites is shown in Fig. 1b.

3.1 *Sample pretreatment*

Samples used for grain size and mineral analyses were treated to remove the organic matter and carbonate, separating the coarse and fine fractions. The procedure was carried out as follows: suitable amounts of sediment sample were placed in a beaker, oxidized and disaggregated by 30% H_2O_2. The above steps were repeated every 12 h until no air bubbles remained to completely remove the organic matter. Then, the solution was desalinated with deionized water and centrifuged a total of 6 times. Afterward, the sample was placed in a water bath box at a constant temperature of 35°C after adding twice sufficient 30% acetic acid, continuously shaking the sample, and repeating the centrifuge procedure. Finally, the carbonate-free fraction was wet-sieved through a 63 μm (240 meshes) sieve. Oversize and undersize subsamples were collected separately to dry them for later use.

3.2 *Grain size analysis*

The grain size distribution of the carbonate-free coarse fraction (>63 μm) was analyzed by a standard sieve shaker test, with a size interval of 1Φ. The relative content of each grain size after weighing was calculated. For the carbonate-free fine fraction (<63 μm), prior to the grain size measurements, subsamples were disaggregated with 3 mL of 0.05 mol/L $(NaPO_3)_6$ and sonicated for 30 min. Grain size distributions were determined using a laser particle size analyzer (Mastersizer 2000, Malvern Company) with a measurement range from 0.02 to 2 000 μm. The grain size detection resolution was 0.01Φ with a relative error of less than 3% during repeated tests. Grain size data were exported based on the detection interval of (1/4)Φ. Finally, the relative proportion for each grain size fraction was computed by normalization. The grading standard was the Udden-Wentworth grade (Udden, 1914; Wentworth, 1922), using the formulas of McManus to calculate grain size parameters (McManus, 1988).

3.3 *Mineralogical analysis of different size fractions*

From the coarse-grained fractions, the microscopic observation and identification were carried out using an OLYMPUS SZ61 stereo microscope. In addition, the morphology of the biogenic component was examined by scanning electron microscopy (SEM, Quanta 200, FEI Company) and energy dispersive spectroscopy (EDS, GENESIS 2000, EDAX Company). The beam spot and work distance of SEM are 5.0 and 10 mm (25 kV, high vacuum mode), respectively, and the magnification varies from 150 to 600. From the fine-grained fractions, the mineral composition was found using the X-ray powder diffraction method with a Bruker D8 ADVANCE diffraction meter produced by Bruker (Germany). Diffraction patterns in the 3°–65° range were obtained using a 0.02° (2θ) step scan and 4°/min scanning speed. Operating conditions were 40 kV and 100 mA using Cu-target radiation. Peak areas were calculated after manual baseline correction using Jade 6.5 software, following the semiquantitative k-value method (Chung, 1974).

4 Results

4.1 *Grain size characteristics of sediments*

Among the carbonate-free fraction of each sample, distinct differences in terms of grain size characteristics are apparent. For the grain size parameters of this fraction, see Table 1. The mean grain size ranges between 1.96Φ and 8.19Φ with a mean of 5.53Φ. The sorting coefficient is 2.07–4.04 with an average of 2.64, indicating its poor sorting generally or even particularly poor sorting for very few samples. The skewness shifts from very positive to very negative, with the value of –2.34 to 3.65. Forty percent of all samples show a majority of fine-grained particles due to the negatively skewed distribution, while others have the opposite grain size composition. The kurtosis is over 2 and the range is 2.47–4.48, which is leptokurtic. Figure 2 illustrates the variation trend in the mean grain size distribution. The finest grain size occurs at SW12 from the north margin of this area, whereas SW10 from the southeast of the ridge axial region shows the coarsest grain size. Generally, the particle sizes in the carbonate-free fraction become slightly smaller from southeast to northwest.

The grain size distribution of the carbonate-free fraction can be summarized in three basic types: unimodal, bimodal and irregular bimodal patterns. Four samples are unimodal with a mode of approximately 1.95–3.91 μm (Fig. 3a). They barely contain the fraction coarser than 500 μm, suggesting an obvious negative skewed distribution. Most samples show a bimodal distribution pattern in which the coarse and fine modal sizes are at 125–250 μm and 1.95–3.91 μm, respectively (Fig. 3b). Some of these samples have a significant positive skewed tendency. Further, the size of the two modes in a very few samples is reversed. In the irregular bimodal pattern, there is little difference in the content of two modes, with a modal size of approximately 500 μm

Table 1. Grain size parameters of the carbonate-free fraction in surface sediments from the SWIR

Sample No.	Mz (Φ)	δ_i	S_{ki}	K_g	Sample No.	Mz (Φ)	δ_i	S_{ki}	K_g
SW1	2.06	2.59	2.95	3.74	SW11	6.41	2.84	–1.41	3.26
SW2	5.27	2.74	2.13	3.24	SW12	8.19	2.36	–2.34	3.24
SW3	5.19	2.85	1.88	3.39	SW13	5.45	4.04	–1.79	4.43
SW4	5.66	2.82	–0.93	3.43	SW14	7.13	2.32	–1.36	2.76
SW5	5.61	2.43	1.62	2.98	SW15	2.58	3.16	3.40	4.30
SW6	6.63	2.37	1.02	2.84	SW16	5.70	3.16	1.73	3.53
SW7	7.05	2.33	–0.90	2.82	SW17	7.11	2.07	0.67	2.47
SW8	3.68	2.44	2.60	3.40	SW18	2.53	2.34	2.68	3.54
SW9	6.94	2.53	–1.43	3.02	SW19	7.24	2.23	–1.10	2.71
SW10	1.96	2.91	3.65	4.48	SW20	8.13	2.33	–2.05	2.99
Average	5.53	2.64	0.55	3.33					

Note: The parameters Mz, σ_i, S_{ki} and K_g indicate the mean grain size, sorting coefficient, skewness and kurtosis, respectively.

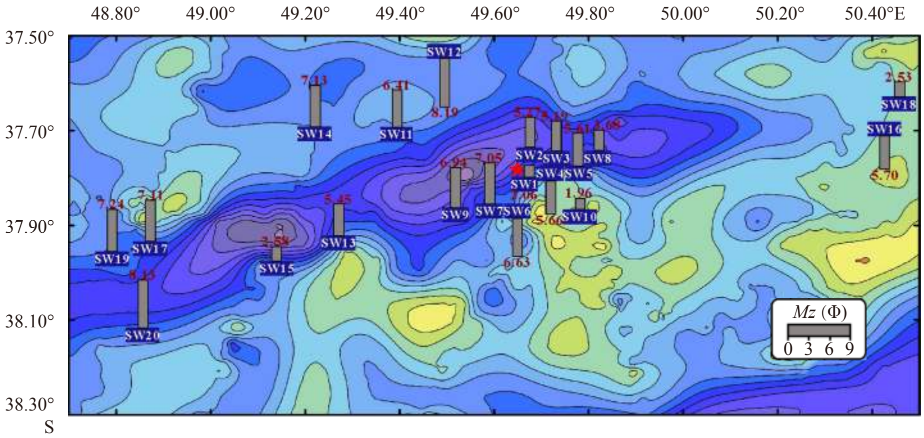

Fig. 2. The mean grain size distribution of the carbonate-free fraction in surface sediments from the SWIR.

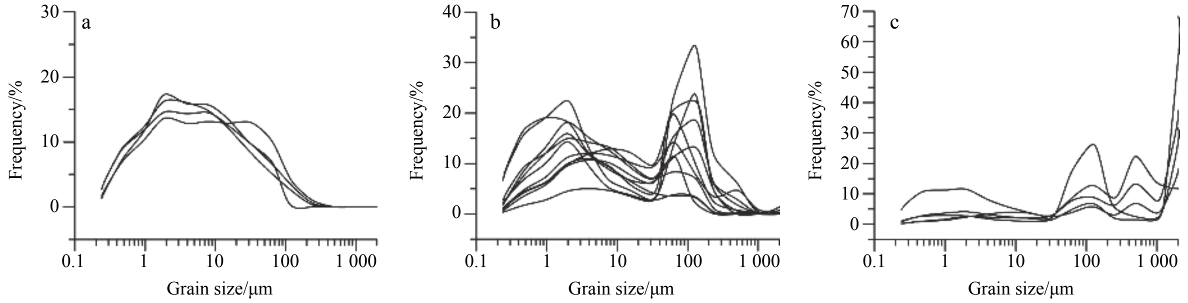

Fig. 3. Grain size distribution patterns of the carbonate-free fraction in surface sediments from the SWIR. Unimodal pattern (a), bimodal pattern (b) and irregular bimodal pattern (c).

and 125 μm, respectively (Fig. 3c). In particular, gravel-grained particles, which have different contents from 11.68% to 68.34%, occur in the >2 000 μm fraction.

4.2 *Mineral phase of different grain size fractions*

Based on the grain size distribution of the noncarbonate fraction, we selected three major coarse-grained fractions for microscopic identification, including >2 000 μm, 500–1 000 μm and 125–250 μm. In the fraction of >2 000 μm, only SW1 approximately 1 km from the 49.6°E hydrothermal field are dominated by massive or fibrous serpentine (Fig. 4a), whereas the remaining gravel-bearing samples, such as SW10, SW13, SW15 and SW18, mainly consist of volcanic breccia and volcanic glass (Figs 4b, c). The volcanic debris grains have an angular shape and develop a vesicular structure, with red-brown partial surface coloration due to iron oxidation.

In the 500–1 000 μm fraction, SW1 still mainly contains serpentine, while individual samples are rich in volcanic glass and volcanic ash, as well as plagioclase and little volcanic matter in certain other samples (Fig. 4d). Of these, plagioclase grains are in angular or subangular shapes and have shallow pits and dark impurities on parts of the surface, with the red-brown color that may be related to oxidation of iron.

In the fraction of 125–250 μm, plagioclase and siliceous bioclasts are generally predominant, with the exception of SW1 and individual samples that are full of volcanic matter. These biogenic components are mainly radiolarian skeletons, followed by siliceous sponge spicules, with intact morphology (Fig. 4e). Through

Fig. 4. Microscope images of the carbonate-free coarse fraction. a. Serpentine; b. volcanic breccia; c. volcanic breccia and volcanic glass; d. volcanic ash, volcanic glass and plagioclase; and e. radiolarians and silica sponge spicules.

comparison of different size fractions, we discover that siliceous bio-clasts are obviously enriched in this fraction such that five samples comprise it almost exclusively: SW4, SW9, SW11, SW12 and SW14.

The XRD results show that 16 mineral phases are detected in the carbonate-free fine fraction (Table 2). The major mineral phases are clay minerals (18%–78%), including chlorite, illite, smectite, and kaolinite, quartz (12%–70%) and plagioclase (3%–32%), which are found at all of the stations, followed by pyroxene. Nontronite, pyrite, serpentine, talc, magnetite and hornblende are discovered at several stations near the hydrothermal field. Sphalerite and epidote are also distributed in areas distant from the field. Barite only appears at SW20, the farthest from the hydrothermal field.

5 The grain size end member model and its genesis

The application of the end member model (Chen and Guillaume, 2012; Paterson and Heslop, 2015) is a powerful approach for interpreting the grain size data in the carbonate-free fraction that is marked by polymodal grain size distribution. According to the numerical-statistical theory of the end member model, we calculated the mean coefficient of determination ($r^2_{\rm mean}$) of all size classes by assuming two to ten end members. The results show that with four end members, the mean coefficient of determination is 0.94, which indicates that four end members can effectively satisfy the fitting requirement (Fig. 5a). When five end members are used, however, the mean coefficient of determination increases slightly ($r^2_{\rm mean}$=0.99) and tends to be generally stable. Therefore, we used four end members to conduct the end member retrieval based on the grain size data. Grain size distributions for four end members (Fig. 5b) reveal that there is a better corresponding relationship in the peak range between each end member and all the samples. The grain size parameters of four end members are provided in Table 3.

EM1 has a unimodal pattern of negative skewed and wider distribution. The particle sizes range from 0.24 to 62.5 μm, with a modal size of 1.95 μm and a mean grain size of 7.65Φ (4.98 μm). Together, this indicates that EM1 basically consists of fine-grained particles. EM2 is characterized by the main peak of higher, sharper and positive skewed distribution. The mode size and mean grain size are 125 μm and 3.77Φ (73.30 μm), respectively. These data show that EM2 is dominated by coarse-grained sediments with small amounts of fine-grained particles. EM3 presents a bimodal pattern of a positively skewed distribution in

Table 2. The contents of minerals in the carbonate-free fine fraction

Sample No.	Clay mineral/%		Sulfide/%		Else/%								
	Chlorite, illite smectite, kaolinite	Nontronite	Pyrite	Sphalerite	Quartz	Plagioclase	Serpentine	Talc	Magnetite	Hornblende	Pyroxene	Epidote	Barite
SW1	48	16			12	3	+++		21				
SW2	23		6	6	33	8	+	7		17			
SW3	39	4	6	7	16	7	+	9		13			
SW4	33	4		5	45	14							
SW5	31		8	3	32	17		3		5			
SW6	20				55	13				9	2		
SW7	22				59	16					3		
SW8	39			13	10	32					3	3	
SW9	29				58	13							
SW10	45				45	8					2		
SW11	76				15	10							
SW12	36				56	8							
SW13	40				51	10							
SW14	18				70	11							
SW15	36			4	29	22					3	5	
SW16	52				41	7							
SW17	42				48	8					2		
SW18	32			6	50	11							
SW19	78				15	5					1		
SW20	63				24	3					4		7

Note: +++ means abundant and + minor. Due to the lack of the *RIR* (reference intensity ratio) (Hubbard et al., 1976) of serpentine it failed to calculate its content.

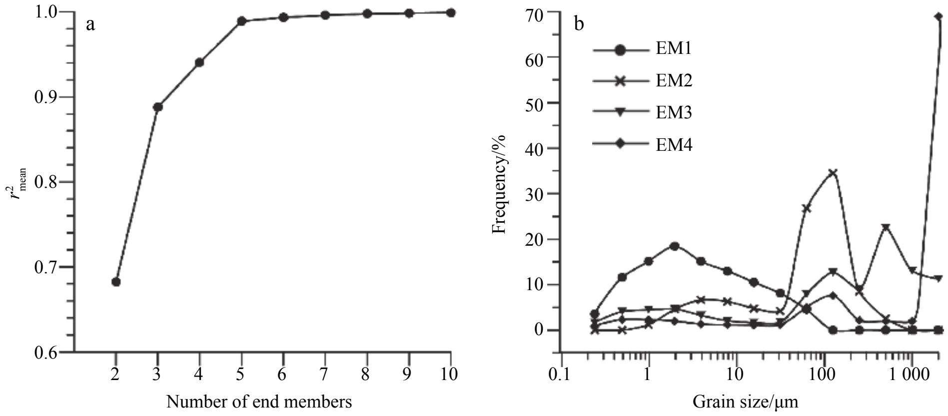

Fig. 5. Grain size end member analysis results of the carbonate-free fraction in surface sediments from the SWIR. Mean coefficient of determination (r^2_{mean}) of all size classes for each end member model (a) and grain size distributions for the end members of the four end member solution (b).

Table 3. Grain size parameters of four end members

No.	*Mz* (Φ)	δ_i	S_{ki}	K_g
EM1	7.65	2.13	-1.17	2.55
EM2	3.77	2.03	2.07	2.75
EM3	2.80	3.42	3.61	4.53
EM4	1.77	2.69	3.52	4.37

which the mode size of the main peak and the secondary peak is 500 µm and 125 µm, respectively. With a mean grain size of 2.80Φ (143.59 µm), overall EM3 is composed of coarser-grained sediments. An irregular bimodal pattern is observed in EM4. The percentage of coarse grains in the secondary peak is less than 8%; however, the percentage of the main peak in which the gravel fraction (>2 000 µm) is dominant in the grain size composition of EM4 is up to 68.97%.

Based on the characteristic of poor sorting in the end members, and considering the fact that sedimentation is influenced by several factors such as provenance, sedimentary environment, hydrodynamic process and biologic activity, to further understand the origin of grain size pattern of the carbonate-free fraction, we focus on the analysis from two aspects: the provenance and transport mechanisms.

5.1 *End member EM1*

The probability distribution of the cumulative grain size can directly and clearly reflect the characteristics of sediment transport and hydrodynamic environment. EM1 is the typical suspended load transport of one segment pattern (Fig. 6a). The total amount of suspended load section is approximately 95%, which corresponds to its relatively wider unimodal distribution. Therefore, it is shown that a large amount of suspended materials falling out from the seawater form the carbonate-free fine fraction in the SWIR surface sediments.

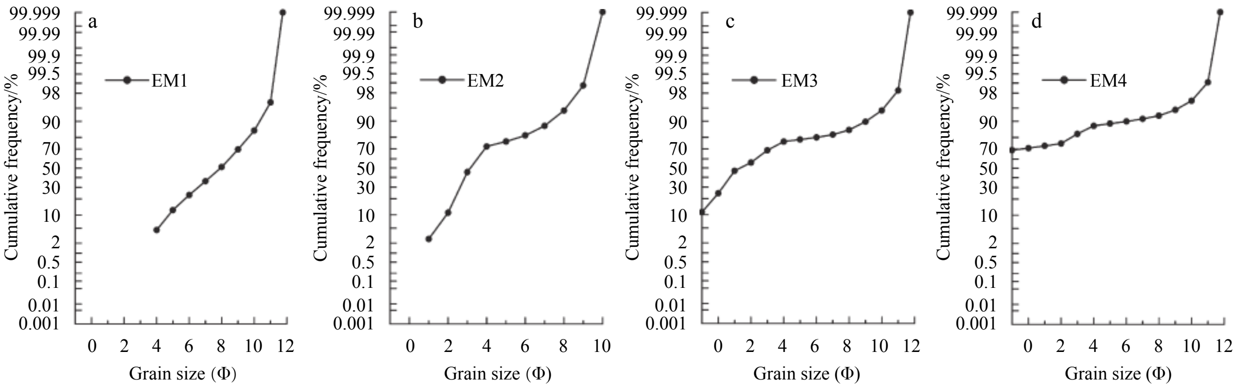

Fig. 6. Probability cumulative grain size distributions for four end members.

This finer end member consists mainly of clay minerals and quartz, with a small amount of silicates, sulfides and sulfate. Clay minerals other than nontronite in the seafloor have three main sources of terrigenous, submarine weathering and hydrothermal origin, which can be transported by wind, bottom current, ice-rafting, and so on (Weaver, 1989). Recent comparative analyses of clay minerals assemblages among different regions have indicated that the major source of clay minerals in the area is aeolian dust from the Namib and Kalahari deserts of southern Africa, as well as some from sediments of Antarctica offshore carried by the Antarctic bottom current①. In addition, clay minerals in sediments near the vent may have hydrothermal origins. Nontronite is found here and it is an indicator mineral (Herzig and Plüger, 1988; Severmann et al., 2004; Dias and Barriga, 2006) related to hydrothermal activity. Quartz is stable at ocean-bottom conditions and does not form authigenically in recent sediments. Most grains in pelagic sediments are in the 5–10 μm range, although the grain size varies with grain origin and transport mechanism (Rex and Goldberg, 1958). The high quartz abundance in the Southwest Indian Ocean is in partially derived from continental material of South Africa and Madagascar and partially derived from the Antarctic continent, as discussed in detail by Kolla et al. (1976b). Thus, the fine-grained quartz distribution within the region is mainly affected by aeolian transport and bottom current processes (Leinen et al., 1986). Closely associated with quartz, plagioclase can exist as terrigenous debris or the weathering debris of basement basalts (Peterson and Goldberg, 1962; Humphris and Thompson, 1978). Pyroxene is one of the major rock-forming minerals of both basalt (Eggleton et al., 1987) and peridotite (Snow and Dick, 1995), and its widespread distribution indicates that it is produced by the bedrock weathering process. Many scholars have noted that the formation of serpentine, magnetite, talc and hornblende near-vent is associated with the alteration (Kelley et al., 2001; Allen and Seyfried, 2003; D'Orazio et al., 2004) and metamorphism (Bonatti et al., 1975) of bedrocks in hydrothermal circulation. Epidote and sphalerite occur at the same time as two stations in this area, which is similar to the results of previous studies on hydrothermal sulfides (Alt et al., 1996; Bowman et al., 1987). Therefore, we suggest that the epidote is likely to be formed at the same time as sphalerite after surrounding rocks suffer from hydrothermal replacement and finally fallout into the sediments. The sulfides distributed around the hydrothermal vent undoubtedly belong to hydrothermal deposits of the 49.6°E hydrothermal field. Tao et al. (2011), Ye et al. (2011), Sun et al. (2014) and Jia et al. (2017) conducted detailed mineralogy studies on chimneys, massive sulfides, upper suspended water, and surrounding sediments, respectively, in this region, and all found pyrite and sphalerite. Barite may be the authigenic deposit most closely associated with primary productivity in the marine sedimentary environment (Sun, 2011).

The above analyses of mineral sources show that EM1 reflects a significant contribution of terrigenous materials of the aeolian and bottom current inputs, although it also contains a few suspended materials related to seafloor weathering and hydrothermal circulation. According to previous research on simulating dust deposition flux using global models, the desert dust aerosol from southern Africa that is dominated by particles of diameter 0.1 to 10 μm, with the mean size being approximately 2 μm could reach the study region in the Southwest Indian Ridge (Jickells et al., 2005).

5.2 *End member EM2*

EM2 has a bi-segment pattern (Fig. 6b) that consists of the bed and suspended load, with a cut-off of 4Φ (62.5 μm). The bed load section, which corresponds to the major mode of EM2, has a higher proportion of up to 70% and slope of approximately 60°, suggesting a slightly better sorting. This end member also has some suspended particles whose the size is the same as that of EM1.

As mentioned above, siliceous bio-clasts are enriched in the fraction of 125–250 μm. This size range is consistent with previous research on the size of radiolarian skeletons in the subtropical region by Schmidt et al. (2006). Through SEM examination, several common species, including *Lamprocyclas maritalis*, *Rhopalastrum hexaceros*, *Stylacontarium octatignum*, *Spongocore polyacantha*, *Octopyle stenozona*, *Acrosphaera spinosa*, *Theopilium tricostatum*, and *Hexalonche philosophica*, were identified in this area. Radiolarians are planktonic protozoa widely distributed throughout the water column in oceans, which are adapted

---

① Zhang Wenqiang, Fan Dejiang, Sun Xiaoxia, et al. The mineral composition and sources of the fine-grainedl sediments from 49.6°E hydrothermal field of the SWIR. Journal of Ocean University of China, https://doi.org/10.1007/s11802-019-3797-6 to a drifting existence. Conversely, sponges are important contributors to benthic biomass in predominantly deep-sea environments and are frequently found on firm surfaces such as rocks or soft sediments. When these creatures die, their skeletal remains make up a part of the cover of the ocean floor as siliceous bioclasts. Thus, this biogenic component in the area belongs to local biogenic deposits. In addition, considering the intact morphology of the shells described previously, we suggest that the study region is in a weak hydrodynamic environment.

5.3 *End member EM3*

Compared with EM2, EM3 has 10% gravel-grained particles that have not experienced any transport process. The bed load section has a wider size range and lower content (58%), whereas the content of the suspended load is unchanged. The secondary part can also be observed in the suspended load (Fig. 6c). This may reflect that the hydrodynamic environment or provenance of this end member has changed.

The 500–1 000 μm fraction sediments are mainly composed of plagioclase, volcanic ash and volcanic glass. EDS analyses show that the coarser plagioclase consists mostly of basic plagioclase (An: 80.20%–85.57%, Ab: 14.57%–19.80% and Or: 0%). Thus, the plagioclase mineral mainly originate from the submarine weathering of basalt rocks. Previously mentioned volcanic activities of ridge segments in this region are intense and of relatively quiet overflow eruption to form seafloor basalts. Consequently, volcanic glass and ash are also the result of volcanic activities or the weathering of basalt rocks.

5.4 *End member EM4*

The remarkable characteristic of EM4 is that the gravel-grained sediments without transport account for 70% of the total. In contrast, the contents of the bed load and suspended load are very low, 20% and 10% (Fig. 6d), respectively. This directly reflects that the water mass movement in this region has no ability to reform gravel-grained or much coarser sediments. Therefore, the distribution of these coarser particles should be closer to their source area.

The gravel-grained fraction in this end member mainly consists of volcanic matter, and with few hydrothermal alteration products, serpentine. The source material between EM3 and EM4 is very similar. It also shows indirectly that the input of volcanic materials makes a large contribution to the coarser-grained sediments in this area. Therefore, EM4 could be interpreted as representing the coarsest volcanic matter from the seafloor bedrocks of the SWIR.

5.5 *The spatial distribution of four end members*

The relative contributions of four end members show distinct spatial variations. All the samples are divided into three types according to their end member contents (Fig. 7). Type 1 includes 55% samples that are mainly composed of EM1. In Type 2, EM2 is the dominant end member. Type 3 is marked by a high proportion of EM3 and EM4.

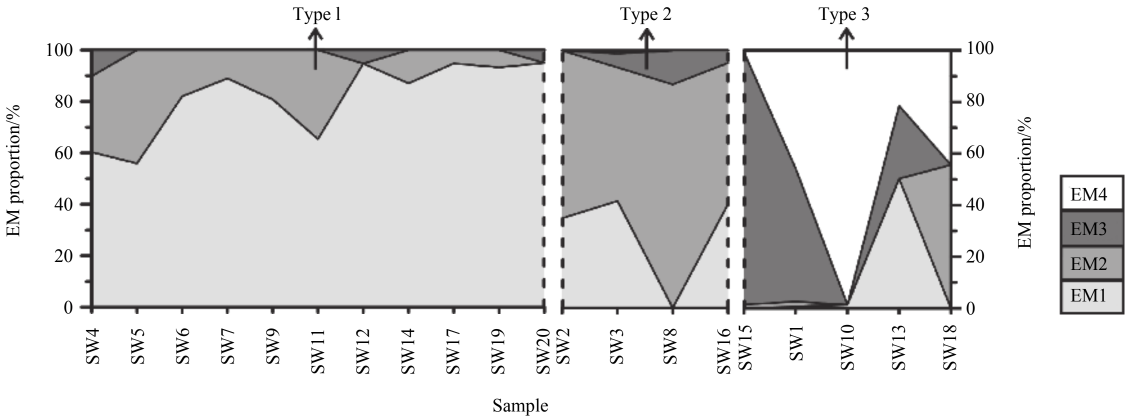

Fig. 7. Distribution of the relative contributions of four end members.

From the wide distribution of samples in Type 1, it is observed and accepted that the aeolian and Antarctic bottom current play the key role in the carbonate-free fine sediments transport in SWIR. In addition, the content of EM1 has an increasing tendency with the distance from the hydrothermal activity field. This trend is thought to be mainly controlled by sediment provenance. On the one hand, the dilution of particles associated with hydrothermal circulation near-vent is relatively clear. These particles contain not only fine suspended settling materials but also coarse hydrothermal alteration products. Further, the coarse particles of volcanic and biogenic sources in EM2 and EM3 also have a dilution effect on EM1. For example, SW5 and SW11 have higher EM2 content. Moreover, the flat areas of the seafloor create beneficial conditions for the accumulation of suspended materials, including hydrothermal components. Due to the lack of actual observation data about topography, there is no further discussion about this aspect.

By combining Type 1 with Type 2, the results show that there was no significant regularity in the spatial distribution of the biogenic component. For how it was created, there are various factors. The biogenic fraction content in marine sediments is related to the supply of biological skeletons in upper or bottom seawater and has a closed relationship with ocean biogenic production controlled by temperature, salinity and hydrological properties of the upwelling current and ocean current. Additionally, siliceous skeletons usually dissolve because of the unsaturated dissolution of silicon dioxide in modern oceanic water. Furthermore, other pelagic sediments can also have a dilution effect on the relative content of biogenic sediment.

The samples in Type 3 have a high content of the coarser (>500 μm) volcanic materials. According to the grain size compositions of four end members, there is nearly 20% basement weathering debris of the coarsest grained materials without transport or reform in the carbonate-free fraction. We believe that such samples provide a better estimate of the sources and average content of the gravel particles in the noncarbonated fraction sediments from the SWIR. Therefore, the concentrated input of endogenous materials, which refers to the volcanic origin, is the main cause of the different spatial distributions of EM3 and EM4.

In summary, the distinct spatial variations of the end members are mainly related to different provenances. Sediments from terrigenous, submarine weathering process of bedrocks, biogenic production and hydrothermal input come together to form a mixed population, such as the carbonate-free fraction of surface sediments in the SWIR. Each origination supplies characteristic mineral suites that contain special grain size information. Therefore, multi-provenance is a major factor influencing the grain size pattern in this fraction. Second, since the entire region has weak hydrodynamic action owing to its deep-sea environment, only the Antarctic bottom current that flows to the northwest can provide a velocity component (Mantyla and Reid, 1995) to transport some of the surface sediments and control their deposition in the seabed. Combined with other indirect transport processes in this region, such as wind, the particle sizes ultimately present a slightly decreasing tendency from southeast to northwest. In addition, other factors such as topography may influence the grain size composition of SWIR surface sediments.

6 Conclusions

Data on grain sizes and mineral compositions of the carbonate-free fraction in surface sediments from the Southwest Indian Ridge provide important information about factors in grain size pattern and can be summarized as follows:

(1) The mean grain size of the carbonate-free fraction ranges in 1.96Φ–8.19Φ with poor sorting. The grain size seems to become slightly finer from the southeast to the northwest in this area. Three types of grain size distributions are distinguished, namely, the unimodal, bimodal and irregular bimodal patterns.

(2) The end member model, EM1, represents the significant contribution of terrigenous materials of inputs of aeolian origin and sediment carried by bottom current inputs. EM2 reflects the influence of sediments of siliceous bio-clasts. EM3 and EM4 are interpreted as representing the coarser (>500 μm) volcanic materials relate to bedrock weathering or volcanic activities.

(3) The sediment sources are different and can be distinguished as terrigenous, volcanic, hydrothermal and biogenic. Additionally, the multi-provenance origin of the sediments is the dominant factor controlling the grain size pattern of the carbonate-free fraction in that area. Sediment transport processes such as the bottom current and wind also exert a minor influence on the pattern.

Acknowledgements

We thank the crew of the R/V *Dayang Yihao* for help in sampling during the DY125-135 voyages.

References

Allen D E, Seyfried W E. 2003. Compositional controls on vent fluids from ultramafic-hosted hydrothermal systems at mid-ocean ridges: an experimental study at 400°C, 500 bars. Geochimica et Cosmochimica Acta, 67(8): 1531–1542, doi: 10.1016/S0016-7037(02)01173-0

Alt J C, Laverne C, Vanko D A, et al. 1996. Hydrothermal alteration of a section of upper oceanic crust in the eastern equatorial Pacific: a synthesis of results from Site 504 (DSDP Legs 69, 70, and 83, and ODP Legs 111, 137, 140, and 148). In: Alt J C, Kinoshita H, Stokking L B, et al., eds. Proceedings of the Ocean Drilling Program, Scientific Results. College Station Texas: Ocean Drilling Program, 148: 417–434

An Zhisheng, Kutzbach J E, Prell W L, et al. 2001. Evolution of Asian monsoons and phased uplift of the Himalaya-Tibetan plateau since Late Miocene times. Nature, 411(6833): 62–66, doi: 10.1038/35075035

Bach W, Banerjee N R, Dick H J B, et al. 2002. Discovery of ancient and active hydrothermal systems along the ultra-slow spreading Southwest Indian Ridge 10°–16°E. Geochemistry, Geophysics, Geosystems, 3(7): 1–14

Bernard A, Munschy M, Rotstein Y, et al. 2005. Refined spreading history at the Southwest Indian Ridge for the last 96 Ma, with the aid of satellite gravity data. Geophysical Journal International, 162(3): 765–778, doi: 10.1111/gji.2005.162.issue-3

Biscaye P E, Eittreim S L. 1977. Suspended particulate loads and transports in the nepheloid layer of the abyssal Atlantic Ocean. Marine Geology, 23(1–2): 155–172

Bonatti E, Honnorez J, Kirst P, et al. 1975. Metagabbros from the Mid-Atlantic Ridge at 06°N: contact-hydrothermal-dynamic metamorphism beneath the axial valley. The Journal of Geology, 83(1): 61–78, doi: 10.1086/628045

Bowman J R, Parry W T, Kropp W P, et al. 1987. Chemical and isotopic evolution of hydrothermal solutions at Bingham, Utah. Economic Geology, 82(2): 395–428, doi: 10.2113/gsecongeo.82.2.395

Cannat M, Rommevaux-Jestin C, Sauter D, et al. 1999. Formation of the axial relief at the very slow spreading Southwest Indian Ridge (49° to 69°E). Journal of Geophysical Research: Solid Earth, 104(B10): 22825–22843, doi: 10.1029/1999JB900195

Chen Weishi, Guillaume M. 2012. HALS-based NMF with flexible constraints for hyperspectral unmixing. EURASIP Journal on Advances in Signal Processing, 2012(1): 54, doi: 10.1186/1687-6180-2012-54

Chen Yuanyuan, Yu Bingsong, Su Xin, et al. 2013. Mineralogical and geochemical characteristics of the calcareous sediments in Southwest Indian Ridge. Geological Science and Technology Information, 32(1): 107–113

Chung F H. 1974. Quantitative interpretation of X - ray diffraction patterns of mixtures. I. matrix - flushing method for quantitative multicomponent analysis. J Appl Cryst, 7: 526–531, doi: 10.1107/S0021889874010387

Cronan D S, Hodkinson R A. 1997. Geochemistry of hydrothermal sediments from ODP Sites 834 and 835 in the Lau Basin, southwest Pacific. Marine Geology, 141(1–4): 237–268

Dias á S, Barriga F J A S. 2006. Mineralogy and geochemistry of hydrothermal sediments from the serpentinite-hosted Saldanha hydrothermal field (36°34′N; 33°26′W) at MAR. Marine Geology, 225(1–4): 157–175

Dick H J B, Lin Jian, Schouten H. 2003. An ultraslow-spreading class of ocean ridge. Nature, 426(6965): 405–412, doi: 10.1038/nature02128

Doeglas D J. 1968. Grain-size indices, classification and environment. Sedimentology, 10(2): 83–100, doi: 10.1111/sed.1968.10.issue-2

D’Orazio M, Boschi C, Brunelli D. 2004. Talc-rich hydrothermal rocks from the St. Paul and Conrad fracture zones in the Atlantic Ocean. European Journal of Mineralogy, 16(1): 73–83, doi: 10.1127/0935-1221/2004/0016-0073

Eggleton R A, Foudoulis C, Varkevisser D. 1987. Weathering of basalt: changes in rock chemistry and mineralogy. Clays and Clay Minerals, 35(3): 161–169, doi: 10.1346/CCMN

German C R, Petersen S, Hannington M D. 2016. Hydrothermal exploration of mid-ocean ridges: where might the largest sulfide deposits be forming?. Chemical Geology, 420: 114–126, doi: 10.1016/j.chemgeo.2015.11.006

Gurvich E G. 2006. Metalliferous Sediments of the World Ocean: Fundamental Theory of Deep-Sea Hydrothermal Sedimentation. Berlin: Springer, 7–201

Hails J R. 1967. Significance of statistical parameters for distinguishing sedimentary environments in New South Wales, Australia. Journal of Sedimentary Petrology, 37(4): 1059–1069

Haine T W N, Watson A J, Liddicoat M I, et al. 1998. The flow of Antarctic bottom water to the southwest Indian Ocean estimated using CFCs. Journal of Geophysical Research: Oceans, 103(C12): 27637–27653, doi: 10.1029/98JC02476

Herzig P M, Plüger W L. 1988. Exploration for hydrothermal mineralization near the Rodriguez triple junction, Indian Ocean. Canadian Mineralogist, 26: 721–736

Huang Dasong, Zhang Xiaoyu, Zhang Guoyin, et al. 2016. Geochemical characteristics of sediments in Southwest Indian Ridge 48.6°–51.7°E. Geological Science and Technology Information, 35(1): 22–29

Hubbard C R, Evans E H, Smith D K. 1976. The reference intensity ratio, I/I_c, for computer simulated powder patterns. J Appl Cryst, 9(2): 169–174, doi: 10.1107/S0021889876010807

Humphris S E, Thompson G. 1978. Hydrothermal alteration of oceanic basalts by seawater. Geochimica et Cosmochimica Acta, 42(1): 107–125, doi: 10.1016/0016-7037(78)90221-1

Jia Qi, Fan Dejiang, Zhang Wenqiang, et al. 2017. Sulfide mineralogy of surface sediments of the Southwestern Indian Ridge and its geological implication. Acta Mineralogica Sinica, 37(6): 725–736

Jickells T D, An Z S, Andersen K K, et al. 2005. Global iron connections between desert dust, ocean biogeochemistry, and climate. Science, 308(5718): 67–71, doi: 10.1126/science.1105959

Kelley D S, Karson J A, Blackman D K, et al. 2001. An off-axis hydrothermal vent field near the Mid-Atlantic Ridge at 30°N. Nature, 412(6843): 145–149, doi: 10.1038/35084000

Kolla V, Bé A W H, Biscaye P E. 1976a. Calcium carbonate distribution in the surface sediments of the Indian Ocean. Journal of Geophysical Research, 81(15): 2605–2616, doi: 10.1029/JC081i015p02605

Kolla V, Henderson L, Biscaye P E. 1976b. Clay mineralogy and sedimentation in the western Indian Ocean. Deep Sea Research and Oceanographic Abstracts, 23(10): 949–961, doi: 10.1016/0011-7471(76)90825-1

Leinen M, Cwienk D, Heath G R, et al. 1986. Distribution of biogenic silica and quartz in recent deep-sea sediments. Geology, 14(3): 199–203, doi: 10.1130/0091-7613(1986)14<199:DOBSAQ>2.0.CO;2

Li Zhenggang, Chu Fengyou, Jin Lu, et al. 2016. Major and trace element composition of surface sediments from the Southwest Indian Ridge: evidence for the incorporation of a hydrothermal component. Acta Oceanologica Sinica, 35(2): 101–108, doi: 10.1007/s13131-015-0678-8

Liang Yuyang, Li Jiabiao, Li Shoujun, et al. 2014. The Magmato-tectonic dynamic model for the Indomed-Gallieni segment of the central Southwest Indian Ridge. Chinese Journal of Geophysics, 57(9): 2993–3005

Liao Guanghong, Zhou Beifeng, Liang Chujin, et al. 2016. Moored observation of abyssal flow and temperature near a hydrothermal vent on the Southwest Indian Ridge. Journal of Geophysical Research: Oceans, 121(1): 836–860, doi: 10.1002/2015JC011053

Mantyla A W, Reid J L. 1995. On the origins of deep and bottom waters of the Indian Ocean. Journal of Geophysical Research: Oceans, 100(C2): 2417–2439, doi: 10.1029/94JC02564

McCave I N, Hall I R. 2006. Size sorting in marine muds: processes, pitfalls, and prospects for paleoflow-speed proxies. Geochemistry, Geophysics, Geosystems, 7(10): Q10N05

McCave I N, Manighetti B, Robinson S G. 1995. Sortable silt and fine sediment size/composition slicing: parameters for palaeocurrent speed and palaeoceanography. Paleoceanography, 10(3): 593–610, doi: 10.1029/94PA03039

McLaren P, Bowles D. 1985. The effects of sediment transport on grain-size distributions. Journal of Sedimentary Petrology (SEPM), 55(4): 457–470

McManus J. 1988. Grain size determination and interpretation. In: Tucker M, ed. Techniques in Sedimentology. Oxford: Blackwell, 63–85

Muller M R, Minshull T A, White R S. 1999. Segmentation and melt supply at the Southwest Indian Ridge. Geology, 27(10): 867–870, doi: 10.1130/0091-7613(1999)027<0867:SAMSAT>2.3.CO;2

Peterson M N A, Goldberg E D. 1962. Feldspar distributions in South Pacific pelagic sediments. Journal of Geophysical Research, 67(9): 3477–3492, doi: 10.1029/JZ067i009p03477

Paterson G A, Heslop D. 2015. New methods for unmixing sediment grain size data. Geochemistry, Geophysics, Geosystems, 16(12): 4494–4506, doi: 10.1002/2015GC006070

Povea P, Cacho I, Moreno A, et al. 2015. A new procedure for the lithic fraction characterization in marine sediments from high productivity areas: Optimization of analytical and statistical procedures. Limnology and Oceanography: Methods, 13(3): 127–137

Rea D K. 1994. The paleoclimatic record provided by eolian deposition in the deep sea: the geologic history of wind. Reviews of Geophysics, 32(2): 159–195, doi: 10.1029/93RG03257

Revel M, Sinko J A, Grousset F E, et al. 1996. Sr and Nd isotopes as tracers of North Atlantic lithic particles: paleoclimatic implications. Paleoceanography, 11(1): 95–113, doi: 10.1029/95PA03199

Rex R W, Goldberg E D. 1958. Quartz contents of pelagic sediments of the Pacific Ocean. Tellus, 10(1): 153–159, doi: 10.3402/tellusa.v10i1.9223

Ruddiman W F. 1977. Late Quaternary deposition of ice-rafted sand in the subpolar North Atlantic (lat 40° to 65°N). Geological Society of America Bulletin, 88(12): 1813–1827, doi: 10.1130/0016-7606(1977)88<1813:LQDOIS>2.0.CO;2

Schmidt D N, Lazarus D, Young J R, et al. 2006. Biogeography and evolution of body size in marine plankton. Earth-Science Reviews, 78(3–4): 239–266

Severmann S, Mills R A, Palmer M R, et al. 2004. The origin of clay minerals in active and relict hydrothermal deposits. Geochimica et Cosmochimica Acta, 68(1): 73–88, doi: 10.1016/S0016-7037(03)00235-7

Skornyakova I S. 1965. Dispersed iron and manganese in Pacific Ocean sediments. International Geology Review, 7(12): 2161–2174, doi: 10.1080/00206816509474192

Snow J E, Dick H J B. 1995. Pervasive magnesium loss by marine weathering of peridotite. Geochimica et Cosmochimica Acta, 59(20): 4219–4235, doi: 10.1016/0016-7037(95)00239-V

Stein R, Grobe H, Wahsner M. 1994. Organic carbon, carbonate, and clay mineral distributions in eastern central Arctic Ocean surface sediments. Marine Geology, 119(3–4): 269–285

Sun Xiaoxia. 2011. Study on the suspended particulate minerals in the water column in the Eastern Equatorial Pacific Ocean and hydrothermal active areas in the Southwest Indian Ocean [dissertation]. Qingdao: Ocean University of China

Sun Xiaoxia, Yang Zuosheng, Fan Dejiang, et al. 2014. Suspended zinc sulfide particles in the Southwest Indian Ridge area and their relationship with hydrothermal activity. Chinese Science Bulletin, 59(9): 913–923, doi: 10.1007/s11434-014-0118-8

Tao Chunhui, Li Huaiming, Huang Wei, et al. 2011. Mineralogical and geochemical features of sulfide chimneys from the 49°39′E hydrothermal field on the Southwest Indian Ridge and their geological inferences. Chinese Science Bulletin, 56(26): 2828–2838, doi: 10.1007/s11434-011-4619-4

Tao Chunhui, Li Huaiming, Jin Xiaobing, et al. 2014. Seafloor hydrothermal activity and polymetallic sulfide exploration on the Southwest Indian Ridge. Chinese Science Bulletin, 59(19): 2266–2276, doi: 10.1007/s11434-014-0182-0

Udden J A. 1914. Mechanical composition of clastic sediments. Geological Society of America Bulletin, 25(1): 655–744, doi: 10.1130/GSAB-25-655

Weaver C E. 1989. Clays, Muds, and Shales. New York: Elsevier Science Publishing Company, 1–449

Wentworth C K. 1922. A scale of grade and class terms for clastic sediments. The Journal of Geology, 30(5): 377–392, doi: 10.1086/622910

Ye Jun, Shi Xuefa, Yang Yaomin, et al. 2011. Mineralogy of sulfides from ultraslow spreading southwest Indian ridge 49.6°E hydrothermal field and its metallogenic significance. Acta Mineralogica Sinica, 31(1): 17–29

Zeng Zhigang. 2011. Submarine Hydrothermal Geology (in Chinese). Beijing: Science Press, 183–546

Zhou Huaiyang, Dick H J B. 2013. Thin crust as evidence for depleted mantle supporting the Marion Rise. Nature, 494(7436): 195–200, doi: 10.1038/nature11842